

JGR Earth Surface

RESEARCH ARTICLE

10.1029/2022JF006777

Key Points:

- The composition and structure of the ice sheet are effectively uncovered by wave-equation-based seismic imaging methods
- We estimate the radial anisotropy of ice and the thickness of firn-air and firn from inverted 2D shear-wave velocities
- We observe a dipping reflector that generates SH reflections at about 1,700 m depth and link it to a rapid enlargement of crystals

Supporting Information:

Supporting Information may be found in the online version of this article.

Correspondence to:

Z. Zhang, zdzhang@mit.edu

Citation:

Zhang, Z., Nakata, N., Karplus, M., Kaip, G., & Yi, J. (2022). Shallow ice-sheet composite structure revealed by seismic imaging near the West Antarctic Ice Sheet (WAIS) Divide Camp. *Journal of Geophysical Research: Earth Surface*, 127, e2023JF006777. https://doi.org/10.1029/2022JF006777

Received 27 MAY 2022 Accepted 23 NOV 2022

© 2022 The Authors. This is an open access article under the terms of the Creative Commons Attribution-NonCommercial License, which permits use, distribution and reproduction in any medium, provided the original work is properly cited and is not used for commercial purposes.

Shallow Ice-Sheet Composite Structure Revealed by Seismic Imaging Near the West Antarctic Ice Sheet (WAIS) Divide Camp

Zhendong Zhang¹, Nori Nakata^{1,2}, Marianne Karplus³, Galen Kaip³, and Jia Yi⁴

¹Massachusetts Institute of Technology, Cambridge, MA, USA, ²Lawrence Berkeley National Laboratory, Berkeley, CA, USA, ³University of Texas at El Paso, El Paso, TX, USA, ⁴China Earthquake Disaster Prevention Center, China Earthquake Administration, Beijing, China

Abstract Small-scale polar ice-sheet composite structures can influence coarse-grained climate models. For example, surface melting can hydro-fracture the ice and may eventually lubricate the base. The drainage process will change the petrophysical properties of the subsurface and is predictable from high-resolution seismic imaging. Ray-based imaging methods, though limited by the approximations made, have mapped seismic velocities in 1D, but have yet to offer definitive information about the lateral heterogeneity. Here we use the wave-equation-based seismic imaging method to estimate shear-wave velocities and to image an englacial reflector in 2D. We use 7-day ambient-noise data recorded by a linear array near the West Antarctic Ice Sheet (WAIS) Divide drilling site to perform the study. We obtain 2D vertical and horizontal shear-wave velocity models and observe a lateral variation of the radial anisotropy along the acquisition line. The inverted velocity model is further used to estimate the thicknesses of firn-air and firn layers. We also observe evident SH reflections and calculate the reflector image using robust zero-offset imaging and a more precise reverse time migration imaging method. The imaged reflector is at about 1,700 m depth and is dipping to the southwest. We anticipate that a porosity change at that depth may cause this englacial seismic discontinuity near WAIS Divide. Our results demonstrate the feasibility of estimating the petrophysical properties of polar ice using seismic methods. We anticipate our work to be further used for understanding ice dynamics and thermodynamics, such as the stability of ice shelves, the retreat of the Antarctic ice sheet, and restoring the paleo-sedimentary environment.

Plain Language Summary Satellite measurements indicate that the West Antarctic Ice Sheet is losing more than 150 cubic kilometers of ice per year and this trend is accelerating. The melted ice will cause a rise in the worldwide sea level and more extreme weather events. Seismic waves, traveling through the shallow and deep ice, contain rich information about the ice velocities and discontinuities, which helps us better understand the glacier structure, melt rates, and processes. We use cutting-edge seismic imaging methods to estimate shear-wave speeds in the top 200 m and to image seismic discontinuities within the ice sheet. These model parameters are then used to estimate the firn-air and firn thicknesses, the ice crystal fabric orientation, and the petrophysical properties, which are critical to evaluating the ice sheet stability and understanding the ice dynamics and thermodynamics.

1. Introduction

Glacial ice is interactive with Earth's climate change. As a complex multiscale medium, its composite structure varies from millimeters to kilometers (Golden et al., 2020). How the small-scale ice structures influence coarse-grained climate models is an ongoing research question. To answer this question, we need to know the physical processes acting on the ice sheet, such as ice dynamics and thermodynamics (Conway & Rasmussen, 2009; Lai et al., 2020; Sergienko, 2022). Seismic surveys record vibrations traveling through rock and ice with their speed and path telling us something about the glacier structure, melt rates and other material properties of the rock and ice (Aster & Winberry, 2017; Roethlisberger, 1972). Seismic imaging is one of the methods that can translate the recorded vibrations into interpretable model parameters such as velocity and layer boundaries of the subsurface. In this study, we estimate the shear wave velocities and structural imaging of ice sheets using the wave-equation based methods. We first calculate the empirical Green's functions from a 1-week continuous recording. We then estimate the shear wave velocities and the radial anisotropy using the conventional 1D dispersion curve inversion method and the wave-equation dispersion spectrum inversion method. We further estimate the thickness of firn and ice using the inverted velocities and the empirical law. We also calculate the structural



imaging using the reflected SH waves and interpret the reflector as a boundary of grain-size change. Finally, we discuss the feasibility of estimating petrophysical properties from multiple component data.

Ambient noise cross-correlation is an effective seismic method to study Earth's structure (Shearer, 2019). Surface waves are generally the strongest signals observed in noise cross-correlation, which makes high-resolution surface wave tomography possible (Hu et al., 2020; Jaxybulatov et al., 2014; Shapiro et al., 2005; Yang et al., 2007). Surface waves are also preferred to investigate seismic anisotropy due to their high signal-to-noise ratio (SNR) and observable dispersion splitting caused by anisotropy (S. X. Zhang et al., 2009; Chaput et al., 2022). Indeed, shear waves enable better constraints on seismic anisotropy in ice sheets compared to P waves (Diez et al., 2016). Surface wave dispersion curve inversion has been widely used for imaging the shallow structures of the Antarctic (Diez et al., 2016; Fu et al., 2021; Picotti et al., 2015; Shen et al., 2018). The derived 1D velocity models are first-order approximations of a heterogeneous Earth. More advanced 2D/3D inversion algorithms such as wave-equation dispersion spectrum inversion (Z.-D. Zhang & Alkhalifah, 2019b) and full-waveform inversion methods (Pan et al., 2021) are then proposed to handle the lateral variations in the near-surface. The main benefits of the wave-equation dispersion spectrum inversion method over traditional 1D inversion methods are that (a) it can handle lateral variations; (b) it avoids picking dispersion curves; (c) it utilizes both the fundamental and higher modes of Rayleigh and Love waves and (d) the inversion can be solved using gradient-based optimization algorithms. Different from the classic waveform inversion method, the proposed inversion measures the difference of the frequency-dependent phase velocity (f-v spectrum). The f-v spectrum retains the important dispersion features and at the same time reduces the inherent complexity of waveforms, which reduces the non-linearity of inversion. We thus adopt the wave-equation dispersion spectrum inversion method to estimate the shear wave velocities of shallow ice sheets.

Cross-correlation of noise in principle can extract the complete Green's function between two stations, including any reflections, multiples, or scattered waves. Body waves detected from noise cross-correlation have also been used to study the deep Earth (Boué et al., 2014; Lin et al., 2013). Horizontally polarized (SH) waves have many advantages over the traditional compressional (P) waves or vertically polarized (SV) waves in imaging layer boundaries (Woolery et al., 1993; J. Li et al., 2019; Mecking et al., 2021). Specifically, SH waves have a shorter wavelength than P waves at comparable frequencies, facilitating a higher spatial resolution. SH waves are also decoupled from P and SV waves in an isotropic medium, incurring a cleaner image. Besides, SH reflections are often better separated from surface waves than P or converted waves in a near-surface imaging setting. In practice, SH waves extracted from ambient noise can penetrate to the deep earth's interior (H. Li et al., 2010; Shearer, 2019) and are also useful for shallow structural imaging (Draganov et al., 2009; Gu et al., 2021; Nakata et al., 2011). In a seismic reflection survey carried out on the Alpine glacier Colle Gnifetti, SH-wave bed reflections fit the ice-core length better than P-wave bed reflections (Diez et al., 2014). But reliable controlled excitation of shear waves is expensive on land and not yet developed in the marine environment (Bakulin & Calvert, 2005). Ambient noise cross-correlation can effectively extract SH-reflections regardless of the environment. In our study, the extracted SH reflections from ambient noise provide unique information about an englacial seismic discontinuity observed at about 1,700 km depth near West Antarctic Ice Sheet (WAIS) Divide Camp.

Seismic data recorded at Earth's surface preserve the time history of seismic waves traveling in the Earth's interior (Levin, 1984). We need cutting-edge processing methods to extract useful geological information from massive seismic observations. Reverse time migration (RTM) is a seismic imaging method to map the subsurface reflectivity using reflected waves. Reverse time migration (RTM) calculates reflector images where the downgoing waves meet the waves that travel up (Claerbout, 1971) and it involves three steps: (a) forward modeling of seismic wavefields through given velocity models and sources as well as (b) backpropagating time-reversed seismic reflections using the same velocity models, and (c) applying the imaging condition (e.g., a zero-lag cross-correlation of forward- and backward-propagated wavefields). As a wavefield-based imaging method, RTM takes complete physics (e.g., elasticity, anisotropy, and attenuation) into consideration and does not have layer-model assumptions often required by ray-based imaging methods. Although the computational cost is also higher than ray-based methods, rapid improvements in computational power and developments in dense array acquisitions make wavefield-based imaging methods possible for solving large-scale imaging problems.

ZHANG ET AL. 2 of 18

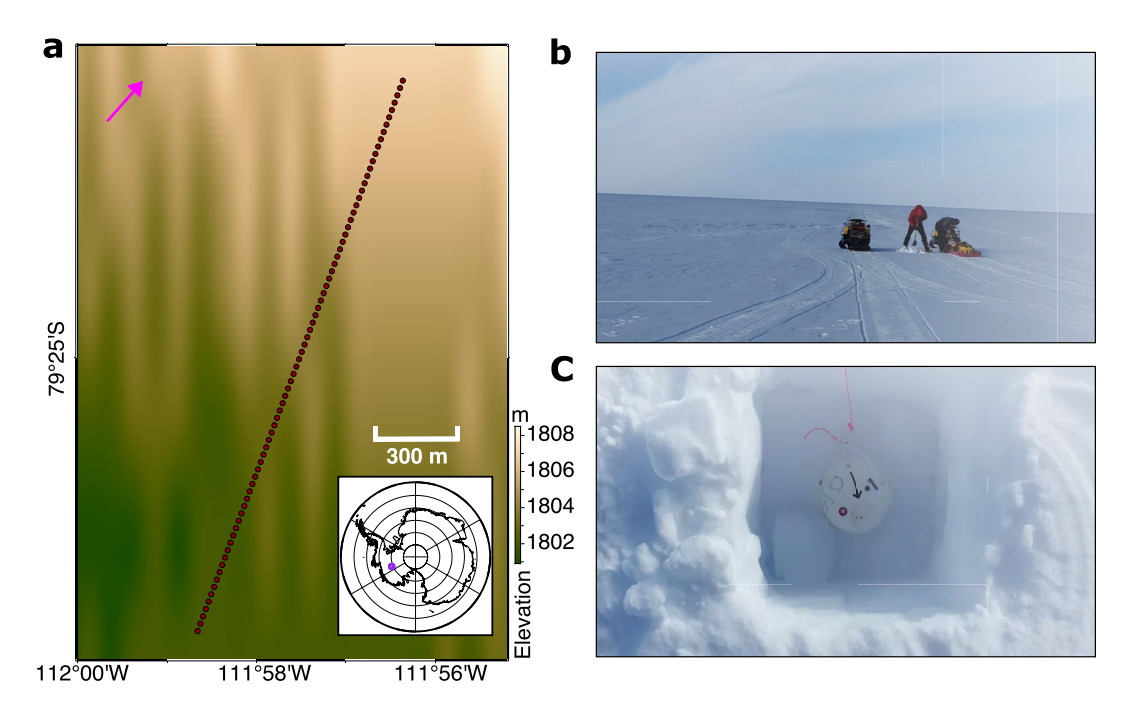


Figure 1. (a) Map of seismic nodes used in this study overlaid with the 1 arc-second global relief and (b) photos from field work showing a team digging a hole for a seismic node and (c) a Magseis Fairfield seismic node deployed in a 30-cm-deep hole. The pink circle in the inset map indicates the location of WAIS Divide Camp. The arrow points to the flow direction (Conway & Rasmussen, 2009). The spatial sampling is 30 m and the total length of the acquisition line is 2.25 km.

2. Study Site

The WAIS is a segment of the continental ice sheet covering the West Antarctic. As a marine-based ice sheet, its bed lies below sea level and its edges flow into floating ice shelves. The WAIS has contributed to significant loss of ice and rise in sea level since the beginning of the twenty-first century, due to the rapid thinning, retreat, and acceleration of major outlet glaciers (Meredith et al., 2019). Geological and glaciological data have been collected to study the asymmetric pattern of thickness change across the divide. The WAIS Divide Core data allow us to learn about the crystal orientation fabric of ice (Fitzpatrick et al., 2014) and to recover the historical Holocene accumulation rate (Koutnik et al., 2016). Seismic surveys, which are more cost-effective than deep ice drilling, are also conducted to study the composite structure of ice near the WAIS Divide drilling site. Similarly, polarimetric ice-penetrating radar measurements are also able to detect anisotropic fabric patterns using birefringence of ice crystals at radar frequencies (Young et al., 2021).

In this study, we use seismic data collected in January 2019 from a temporary deployment located about 5 km northeast of the WAIS Divide Camp and extending about 2.5 km along-flow toward the Walgreen Coast. The deployment consists of 100 3-component, Z-Land Gen2, 5 Hz Magseis Fairfield seismic nodes (Ringler et al., 2018). Nodes were buried at 30 cm depth, leveled with a bubble level, and oriented using an Antarctica-weighted Brunton compass. The nodes recorded continuously with a sampling rate of 1,000 samples per second. Seventy-six nodes were deployed along a 2.25-km-long line with 30-m spacing as shown in Figure 1. Twenty-four nodes deployed in a 500-m diameter circle at the same time are the subject of other studies (Chaput et al., 2022). These seismic node configurations were designed to record controlled seismic source tests during January 2019 (Karplus et al., 2019), but they are also very useful for passive seismic studies, as we show in this paper. The seismic line used in this study follows the same location as a previous controlled-source seismic reflection line collected in 2008–2009 (Horgan et al., 2011, Figure 1b) and is partially colocated with a radar line collected in 2020 (Young et al., 2021).

ZHANG ET AL. 3 of 18

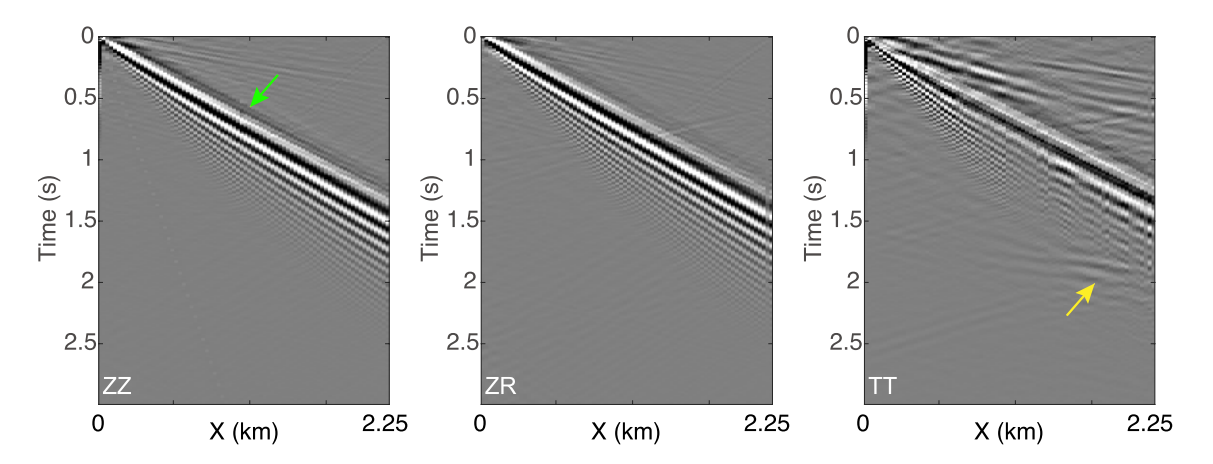


Figure 2. Example of virtual-shot gathers constructed using vertical-vertical (ZZ), vertical-radial (ZR) and tangential-tangential (TT) components. ZZ and ZR data are Rayleigh wave dominated and TT data are Love wave dominated. A notable trace anomaly (no. 38) marked by the green arrow is observed from ZZ data. The TT data look noisier than ZZ and ZR data but have clear reflections marked by the yellow arrow.

3. Data Processing

We have a 1-week continuous recording of ambient noise on the line of Magseis Fairfield 3-component nodes. We calculate the node-to-node correlations of vertical-vertical (ZZ), vertical-radial (ZR) and transverse-transverse (TT) data components. Specifically, the sequential processing steps are (a) instrument response removal, (b) time-domain trace normalization $(\hat{d}(t) = d(t)/|d(t)|)$, (c) spectral whitening $(\hat{D}(\omega) = D(\omega)/|D(\omega)|)$, 1 Hz $< \omega <$ 38 Hz), (d) cross-correlation calculated in the frequency domain (Bensen et al., 2007) and (e) time-domain waveform-similarity weighted stacking (Z.-D. Zhang et al., 2020). Figure 2 shows example virtual shot gathers of ZZ, ZR and TT components, respectively. Rayleigh waves are mainly reconstructed from the ZZand ZR-component data, while Love waves are primarily recorded in the TT-component data according to their particle motion difference. There are also body waves that are weak in amplitudes compared with surface waves. The TT-component data seem to have relatively stronger body waves and noise than the ZZ- and ZR-component data. We also observe a trace with an anomalously late arrival time for the ZZ-component data (marked by a green arrow in Figure 2). We continue with calculating the horizontal and the vertical particle velocity ratio (H/V ratio) of traces that are close to that trace. As shown in Figure 3, the trace with traveltime anomaly (black line) shows a different H/V ratio with its neighboring traces for different (virtual) sources. In contrast, its neighboring traces on both sides share similar H/V ratios. The H/V ratio difference may attribute to the site effects according to Sylvette et al. (2006). We will investigate the cause of such a difference in the 2D inversion section. We then calculate the frequency-slowness spectra of the ZZ- and TT-component data in the following way: (a)

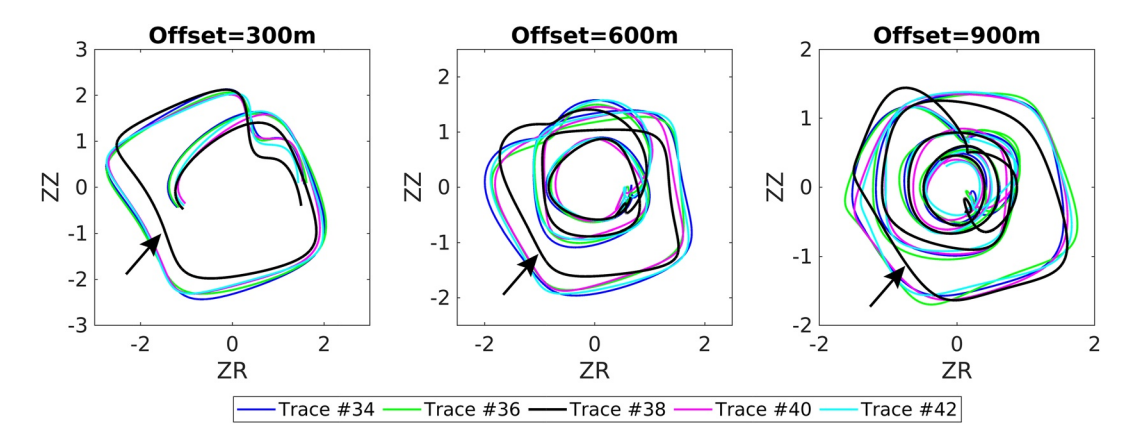


Figure 3. H/V ratio of the marked trace in Figure 2 and its neighboring traces. We choose short (300 m), medium (600 m) and large (900 m) offsets away from the virtual source for visualization. The selected traces are fixed while the virtual sources are varying. They suggest that the 38th trace shows a different H/V ratio from its neighboring traces.

ZHANG ET AL. 4 of 18

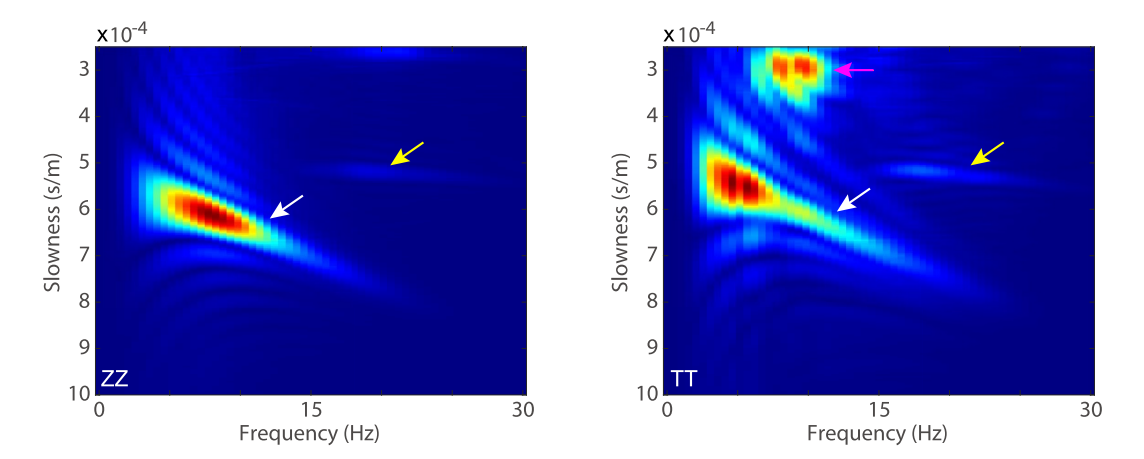


Figure 4. Example frequency-slowness spectra of the ZZ and TT data shown in Figure 2. Rayleigh and Love waves are clearly shown in ZZ and TT data (white arrows), respectively. The yellow arrows point to weak body S-waves with a velocity of around 2 km/s. A cloud of energy with high velocity (about 3.3 km/s) marked by a magenta arrow is identified in TT data. It is well separated from the Love wave in slowness.

We decompose the time-domain data to mono-frequency components. (b) We use the slant stacking to convert the data in the frequency-offset domain to their dispersion spectra in the frequency-slowness domain. We calculate the spectra using traces at least 300 m away from the virtual shot trace. As expected, we observe strong fundamental modes of Rayleigh and Love waves from the frequency-slowness spectra of ZZ and TT data, respectively. There are also weak SV and SH body waves pointed to by the yellow arrows. We also observe relatively strong waves with a phase velocity of about 3.3 km/s, which could be the leaking mode of *P* waves and are not used for inversion.

4. 1D Dispersion Curve Inversion

We pick the Rayleigh and Love wave dispersion curves from frequency-slowness spectra of ZZ- and TT-component data as shown in Figure 4, respectively. The picker seeks the slowness corresponding to the peak amplitude at each frequency. We use the inversion algorithm developed by Haney and Tsai (2017), which assumes a layered Earth, to estimate the 1D velocity profiles. The inversion is based on weighted-damped least squares and thus effectively generates smoothly varying velocity estimation in depth. We start with linearly increasing velocity and density models and keep P-wave velocity and density fixed during the inversion. Figure 5a shows the initial and inverted 1D vertical shear-wave velocities. A low-velocity (<1,400 m/s) layer at shallow depths (<30 m) is reconstructed after inversion. The inverted velocities increase with depth and become almost constant at depths greater than 100 m. The inverted velocity model overall agrees with the published velocity models in the Western Antarctic (Diez et al., 2016; Picotti et al., 2015). The data comparison shown in Figures 5c and 5d indicate that the inversion algorithm does a decent job of matching the observed dispersion curve. Data residuals at both ends of frequencies (lower than 1.5 Hz or higher than 25 Hz) are minor. The limited span of nodes (about 2.5 km) and relatively sparse node sampling (about 30 m) cast the lower and upper limits for resolvable surface waves. It requires that the lowest frequency should be above 1 Hz to record one cycle of the surface waves. Meanwhile, the frequency should be lower than 20 Hz to avoid data aliasing (i.e., at least two nodes per wavelength, assuming the shallow velocity is 1,200 m/s). The sensitivity kernel of the Rayleigh wave (Figure 5b) provides a way to evaluate the accuracy of the inverted velocity model. Higher data sensitivity usually means a more reliable reconstruction of the velocity model at that depth. The inversion progressively boosts the weak data sensitivities, and thus, we can have model updates in depths below 100 m in this example. However, the estimated velocity in such depth is more vulnerable to noise and other factors that may contaminate the velocity model.

We use the inverted vertical shear-wave velocity as the starting model for the Love wave dispersion curve inversion. As shown in Figure 6, the velocity discrepancy indicates radial anisotropy on this site. Shear waves propagate faster in the vertical direction than in the horizontal direction in the upmost few meters (<10 m). The fast-propagation direction becomes horizontal below around 10 m depth, which is reasonable for gravity sedimentary and crystalline fabric of ice. This observation also agrees with the findings from Picotti et al. (2015).

ZHANG ET AL. 5 of 18

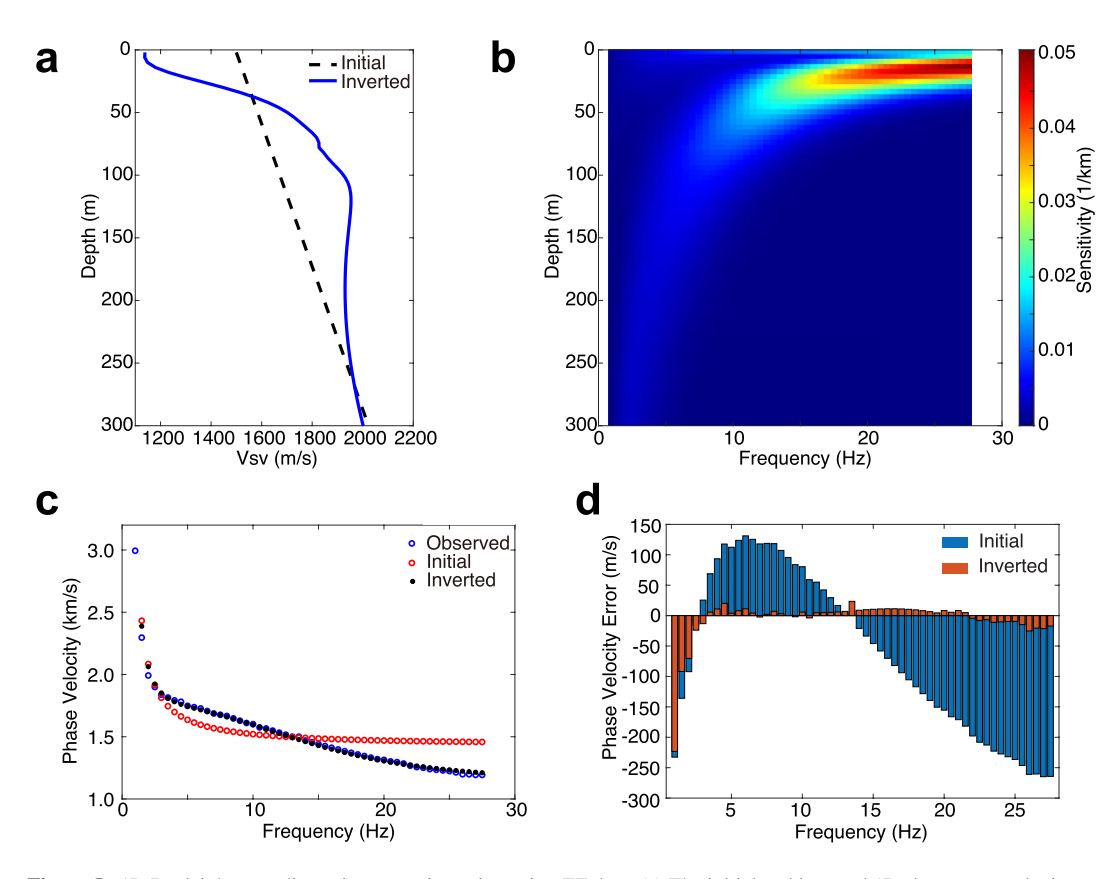


Figure 5. 1D Rayleigh wave dispersion curve inversion using ZZ data. (a) The initial and inverted 1D shear-wave velocity. (b) The depth sensitivity of Rayleigh waves. (c) The observed, initially- and finally-predicted dispersion curves. (d) Phase velocity mismatch before and after inversion. A significant mismatch between observed and inverted phase-velocity dispersion curves at low frequencies may be reasonable due to the limited survey line.

However, the estimated Vsh in depths below 100 m is presumably larger than the actual values, as indicated by the data mismatch at low frequencies shown in Figures 6c and 6d. The predicted dispersion curve is slightly higher than the observed one below 5 Hz, which indicates that the velocity is likely overestimated below 100 m (the penetration depth is about one-third of the wavelength). This data residual, of course, can be further reduced by lifting the model regularization. However, we need the model regularization to avoid data overfitting, especially for real data applications. The Love wave data sensitivity (Figure 6b) reduces rapidly as depth increase, which indicates that the estimated Vsh has a large uncertainty beyond 200 m depth. Besides, the TT-component data are also noisy, preventing a more exact data fitting.

1D dispersion curve inversion, as a widely used inversion method, provides some insights into the velocity structure averaged along the line. However, it also sacrifices the lateral resolution to the subsurface. Though a fine-tuned pseudo-2D inversion (e.g., multiple 1D profiles along a line) can add some lateral variations (Zigone et al., 2015), the layer-model assumption is still a strong approximation for heterogeneous earth. In the next section, we will apply the 2D wave-equation-based dispersion spectrum inversion method to the data set, which considers the more complete physics of wave propagation.

5. 2D Wave-Equation Dispersion Spectrum Inversion

The wave-equation dispersion curve inversion method was introduced by Z.-D. Zhang et al. (2015). The idea is to replace the multilayer dispersion computation (Haskell, 1953) with more advanced wave-equation solutions, where a heterogeneous model can be used. Later, Z.-D. Zhang and Alkhalifah (2019b) replaced the picked dispersion curves with the whole dispersion spectrum as the input data and derived the formula for gradient calculation. The inversion method becomes practically useful for processing large-volume data sets and has been used for solving problems across scales (Z.-D. Zhang et al., 2021). The workflow is similar to the widely used

ZHANG ET AL. 6 of 18

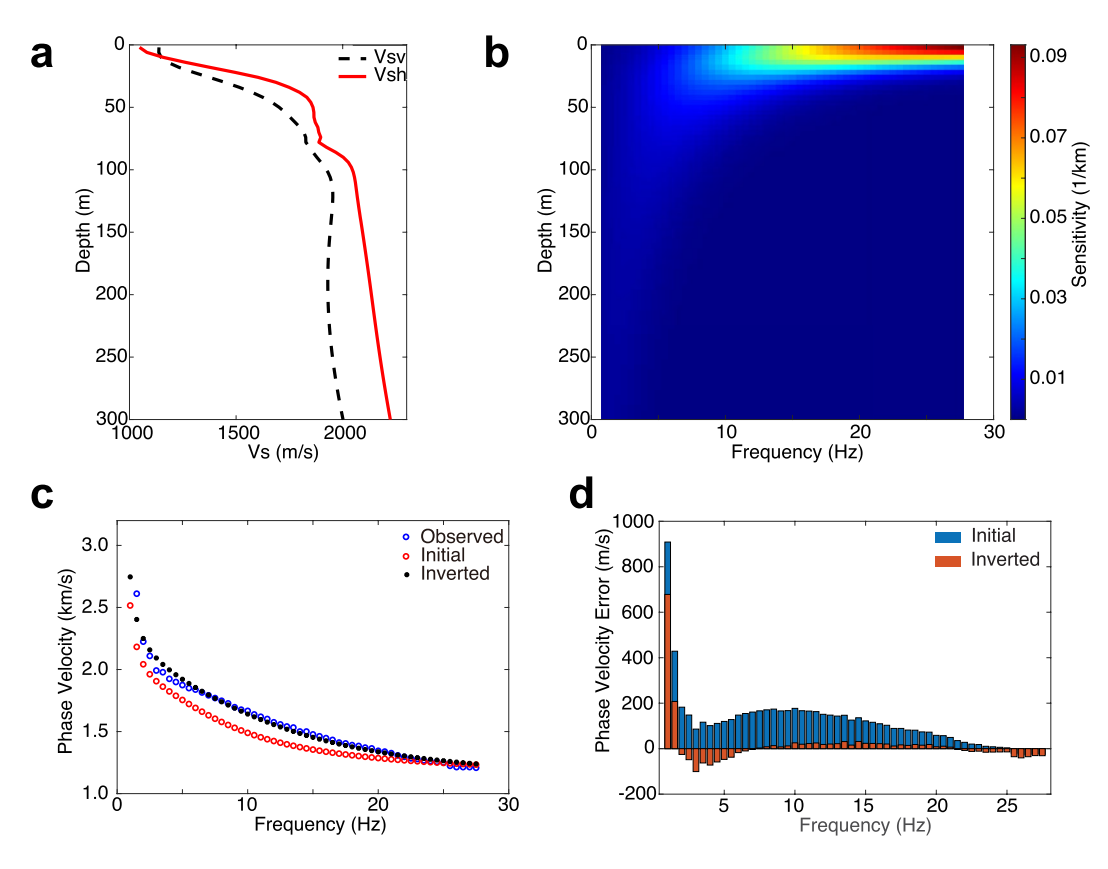


Figure 6. 1D Love wave dispersion curve inversion using TT data. (a) The inverted 1D shear-wave velocities from ZZ and TT data, respectively. The inverted Vsv velocity, as shown in Figure 5 is used as the starting model for Vsh velocity inversion. (b) The depth sensitivity of Love waves. The uncertainty of inverted Vsh velocity may increase rapidly with depth. (c) The observed, initially- and finally-predicted phase-velocity dispersion curves. (d) Phase velocity mismatch before and after inversion.

conventional full-waveform inversion except for a customized objective function—a local similarity measurement of the predicted and observed f- ν spectra. After obtaining the virtual common-shot-gathers, we first transform the time-domain waveform data to the frequency domain (f- ν data, ν denotes offsets) and then calculate their dispersion spectra (f- ν) using the linear Radon transform (Luo et al., 2008). By maximizing the local similarities between the predicted and f- ν spectra, we obtain the optimal shear-wave velocity estimation for the subsurface (Z.-D. Zhang & Alkhalifah, 2019b).

We solve the seismic wave propagation problem using the spectral element method (Komatitsch & Tromp, 1999). We first estimate the vertical shear-wave velocity using Rayleigh waves convoluted with Ricker wavelets with peak frequencies of 8 and 12 Hz, sequentially. We choose these frequencies for the following reasons: (a) the calculated empirical Green's functions have a peak frequency of around 8 Hz and (b) the length and receiver sampling of the array suggest low and high limits for the useful frequencies. The array should record 2-3 cycles of surface waves for a reliable calculation of the f-v spectra and meanwhile, one cycle of surface waves should be recorded by at least two receivers to avoid aliasing (Foti et al., 2018). The source wavelet used for forward modeling is the time integral of the Ricker wavelet with the same peak frequency. Notably this will implicitly apply a time derivative to the calculated empirical Green's functions. A point-source to line-source correction is also applied to transform seismic data recorded in a 3D real world to a 2D computation domain (Pica et al., 1990). The shear-wave velocity is updated iteratively using the limited-memory Broyden-Fletcher-Goldfarb-Shanno (I-BFGS) algorithm (Liu & Nocedal, 1989). The inversion converges in 2 hr with eight computation nodes and each node is equipped with 40 threads. Figure 7 shows the inverted shear-wave velocities using 76 virtual shot gathers. The history of velocity model updates is also provided in the Supporting Information Figure S1. The inverted Vsv model also indicates a low-velocity layer (<30 m) on top of an almost constant velocity layer (about 2 km/s). The lateral variation is mild as we can expect for the ice sheet. Following the inversion strategy we used

ZHANG ET AL. 7 of 18

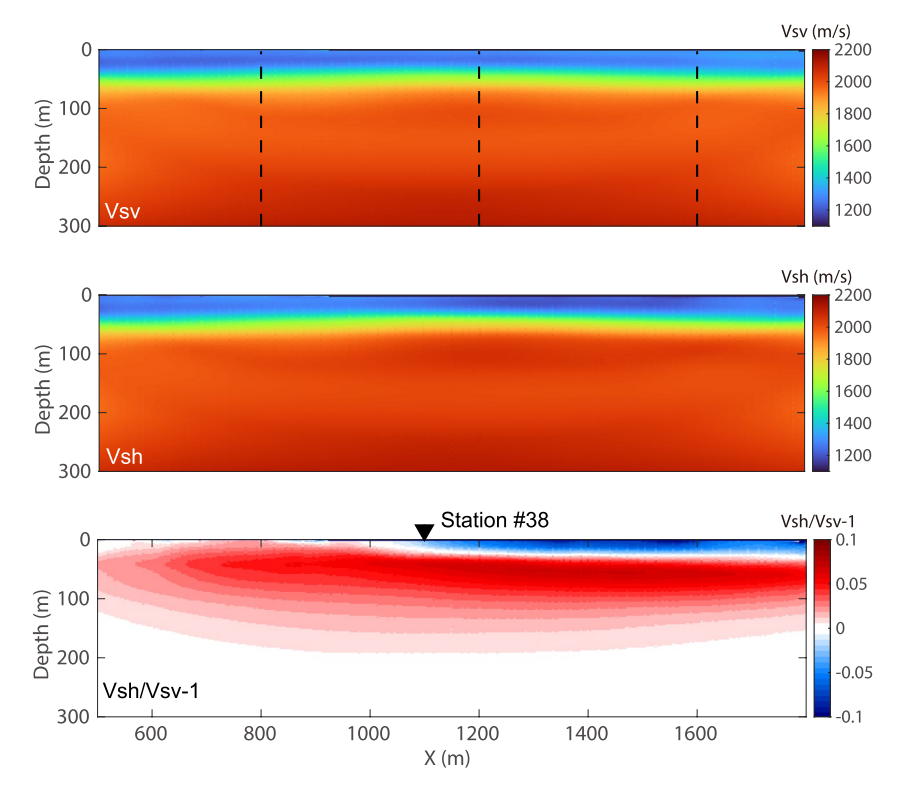


Figure 7. Inverted vertical and horizontal shear wave velocities and their ratios using the 2D inversion method. Both inverted Vsv and Vsh velocities show a low-velocity layer in the upper 30 m and mild lateral variations. The ratio of horizontal and vertical velocities shows an evident lateral change near the 38th station, where we observe a trace anomaly in Figure 2. Three vertical profiles located at the dashed lines are also extracted for further analysis.

in the 1D inversion, we use the inverted Vsv model as the input for the Love wave inversion. The inverted Vsh model is quite close to the starting model and has no significant updates below 200 m (e.g., Vsh/Vsv $-1 \approx 0$ in Figure 7). We also measure the radial anisotropy using the Vsh and Vsv ratio. An interesting observation is that the measured radial anisotropy shows evident lateral variations in the shallow layer. The transition point is coincidentally close to the anomaly trace we observed from the ZZ data (Figure 2). The inverted Vsh is in general greater than Vsv and the maximum velocity difference is about 8%. There is no significant difference in Vsh and Vsv at depths below 200 m due to the vanished Love-wave data sensitivity. For a better comparison, we also extract three vertical profiles at different lateral locations marked by dashed lines in the 2D inversion results. As shown in Figure 8, the estimated velocities using the 2D inversion are not far from those obtained from a 1D inversion due to the mild lateral variation in this region (see the Supporting Information Figure S1 for a direct comparison). The derived radial anisotropy in the firn layer can be strongly heterogeneous due to the variable and often loose compaction of the snow. The ice layer presents a consistent radial anisotropy due to the layering of ice. The horizontal shear wave velocity is always larger than the vertical one. The directional velocity difference has a maximum of 8% and also varies laterally. There is not much difference between horizontal and vertical S-wave velocities beyond 200 m because of the reduced data sensitivity at those depths.

6. Firn-Air Thickness Estimation

Following the work of Diez et al. (2014), we further estimate the top of the ice and the thickness of firn-air content from the inverted S-wave velocities. The first step is to convert the estimated S-wave velocity to density using their empirical relationship (Diez et al., 2014),

$$\rho(z) = \frac{\rho_{ice}}{1 + \{(V_{s,ice} - V_s(z))/950\}^{1.17}},$$
(1)

ZHANG ET AL. 8 of 18

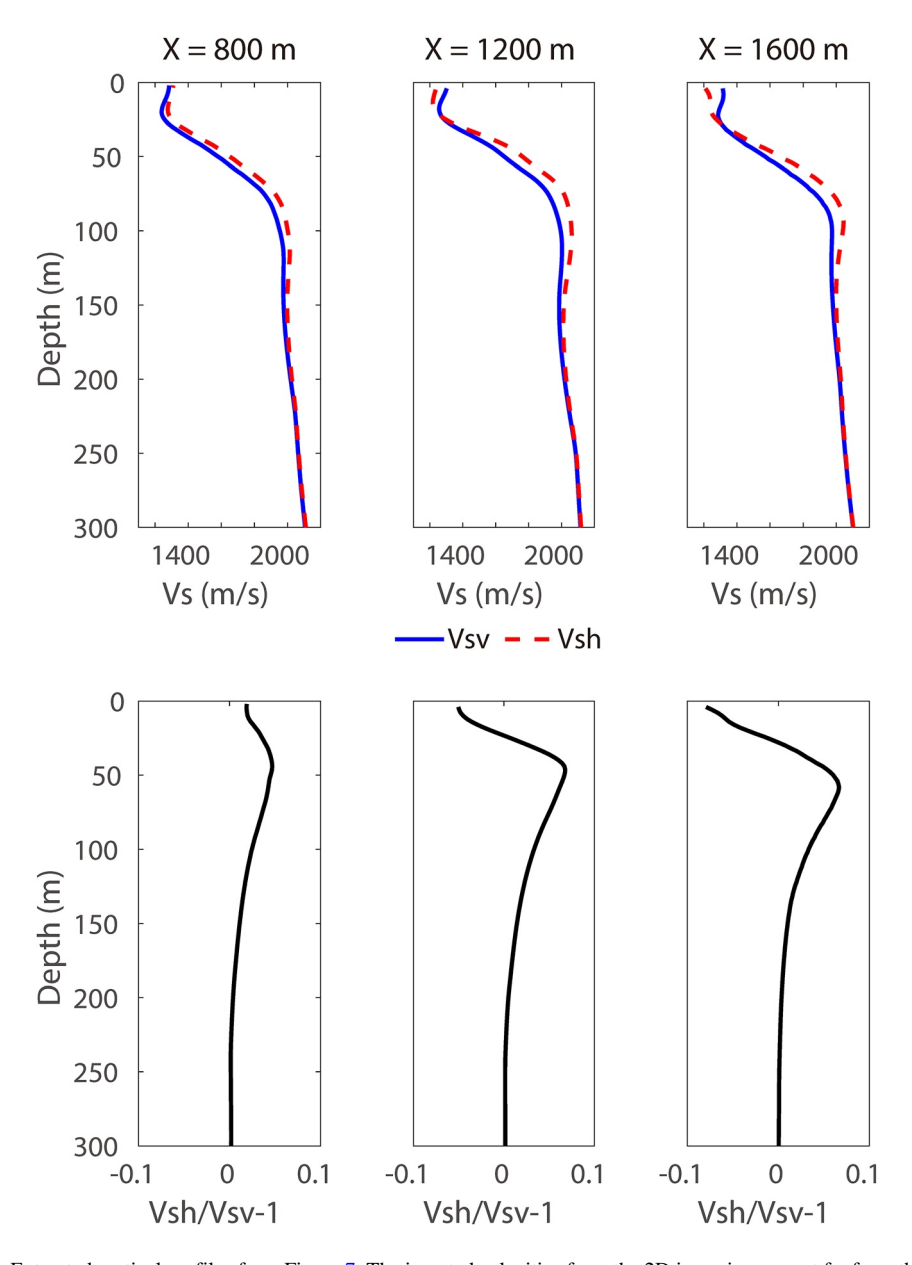


Figure 8. Extracted vertical profiles from Figure 7. The inverted velocities from the 2D inversion are not far from those inverted from the 1D inversion. The lateral variation of shear wave velocity is mild in this region. However, the horizontal and vertical velocity ratio shows a more significant change with locations. A transition from a positive radial anisotropy ratio (Vsh > Vsv) to a negative value (Vsh < Vsv) for the upper 30 m happens near the 38th trace location. The layer composed of firn (30–150 m) always has a more higher shear wave velocity in the horizontal direction. The deep layer shows no clear velocity difference in the vertical and horizontal directions, which is significantly different from the 1D inversion.

where ρ_{ice} and $V_{s,\text{ice}}$ are density and S-wave velocity of ice, respectively. We use a typical value of 900 kg/m³ for ice density. We use a 1D S-wave velocity, which is an average of vertical and horizontal S-wave velocities as shown in Figures 7a and 7b, as $V_s(z)$. The S-wave velocity for ice ($V_{s,\text{ice}} = 1,930 \text{ m/s}$) is picked from depths around 100 m, where the inverted velocity is almost constant.

The firn basement is at the pore close-off depth, that is, a density of 830 kg/m³. The depth of firn basement is at a depth of approximately 62 m. In comparison, Battle et al. (2011) estimated the total firn thickness to be about 67–77 m at WAIS Divide by analyzing collected air samples from two holes (WDC05-B and WDC05-C). Diez et al. (2016) measured a firn thickness of 47 m at Ross Ice Shelf using the empirical law and 1D velocities. The firn-air content thickness can be approximated by

ZHANG ET AL. 9 of 18

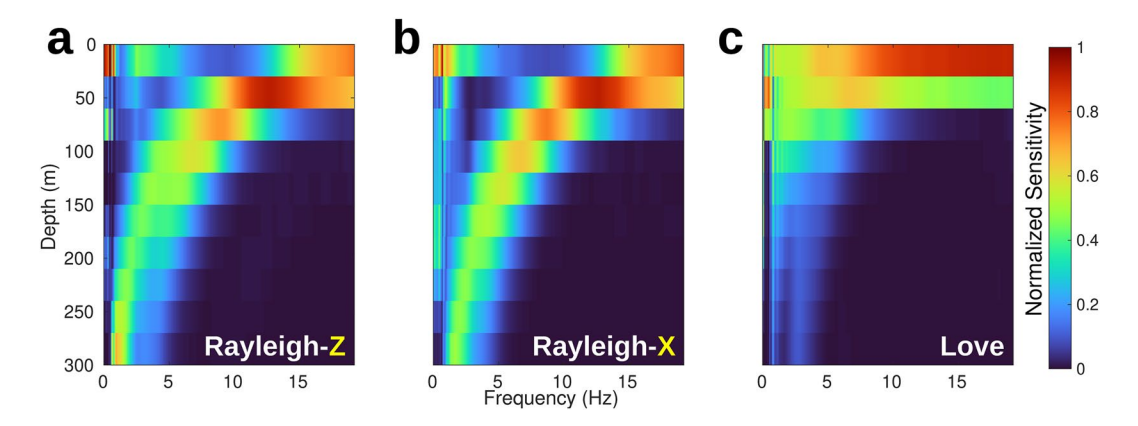


Figure 9. Normalized depth sensitivities of the proposed 2D inversion using (a) *Z*- and (b) *X*-component Rayleigh waves and (c) Love waves. They generally agree with results from 1D inversion analysis (i.e., Figures 5c and 6c) and provide evaluations for the inverted *S*-wave velocities based on the availability of frequencies in the observed data.

$$f_t = \sum_{z=0}^{i_t} \left[1 - \frac{\rho(z)}{\rho_{ice}} \right]. \tag{2}$$

We use the ice depth of 62 m and obtain the firn-air content thickness, which is about 17 m. Our finding is in good agreement with Munneke et al. (2014) and Diez et al. (2016), who modeled firn-air content thickness to be about 20 and 18 m, respectively, on the Ross Ice Shelf. The firn-air content thickness is a key factor in assessing ice-shelf stability. Although our study area is on an ice-sheet, the proposed method can be easily applied to seismic data collected on ice shelves.

7. Inversion Uncertainty Analysis

It is important to know which features of the inverted 2D models are well resolved and thus are reliable. In this study, we are particularly interested in knowing the maximum resolvable depth of the inverted *S*-wave velocities. Checkerboard tests and point-spread function tests are two traditional uncertainty quantification methods that can do this task. However, they also suffer from huge computational demand and limited spatial resolution. Alternatively, we use a finite-difference approximation to calculate the depth sensitivity of Rayleigh and Love waves' dispersion spectra, also known as the Frechét derivatives. Specifically, we first divide the inverted *S*-wave velocities (Figures 7a and 7b) into 10 layers and assign 10% perturbations to each layer. Then we calculate the synthetic waveform data using the background and perturbed models. Finally, we quantify the dispersion spectrum perturbations caused by *S*-wave velocity perturbations at variable depths for frequencies of interest. Figure 9 shows the calculated depth sensitivities of Rayleigh and Love waves used in this study. In general, high-frequency data are sensitive to a shallow depth and vice versa. Love waves are more sensitive to a shallower depth than Rayleigh waves at the same frequencies. These observations agree with the results from traditional 1D inversions (Figures 5c and 6c). From the available frequencies (i.e., about 5–15 Hz from Figure 4), we confirm that the inverted velocities (e.g., Figure 7) are robustly constructed in the top 200 m. The vanished radial anisotropy below 200 m depth is more likely caused by the reduced depth sensitivity of Love waves.

We then show the history of data convergence for each inversion stage in Figure 10. The inversion stops when there are no significant updates. No gold standard exists for an acceptable misfit reduction in real data applications. But the data misfit reduction in our case is sufficient compared to a real-data example (e.g., Figure 14 in Vigh et al. (2014)). We further compare the dispersion spectra and waveforms before and after inversion to better understand the data agreement. Notably, the waveform data are not directly used by the inversion algorithm and thus can indicate whether the inversion has a balanced data fitting. Figure 11 shows the Rayleigh wave dispersion spectra of the observed, initially predicted and finally predicted ZZ- and ZR-component data, respectively. The predicted dispersion spectra from the inverted shear-wave velocity match the observed ones reasonably well. The objective function used for inversion focuses on matching the curvature of the dispersion spectrum. This is reasonable for real data applications because the amplitude can be influenced by many factors that are not

ZHANG ET AL. 10 of 18

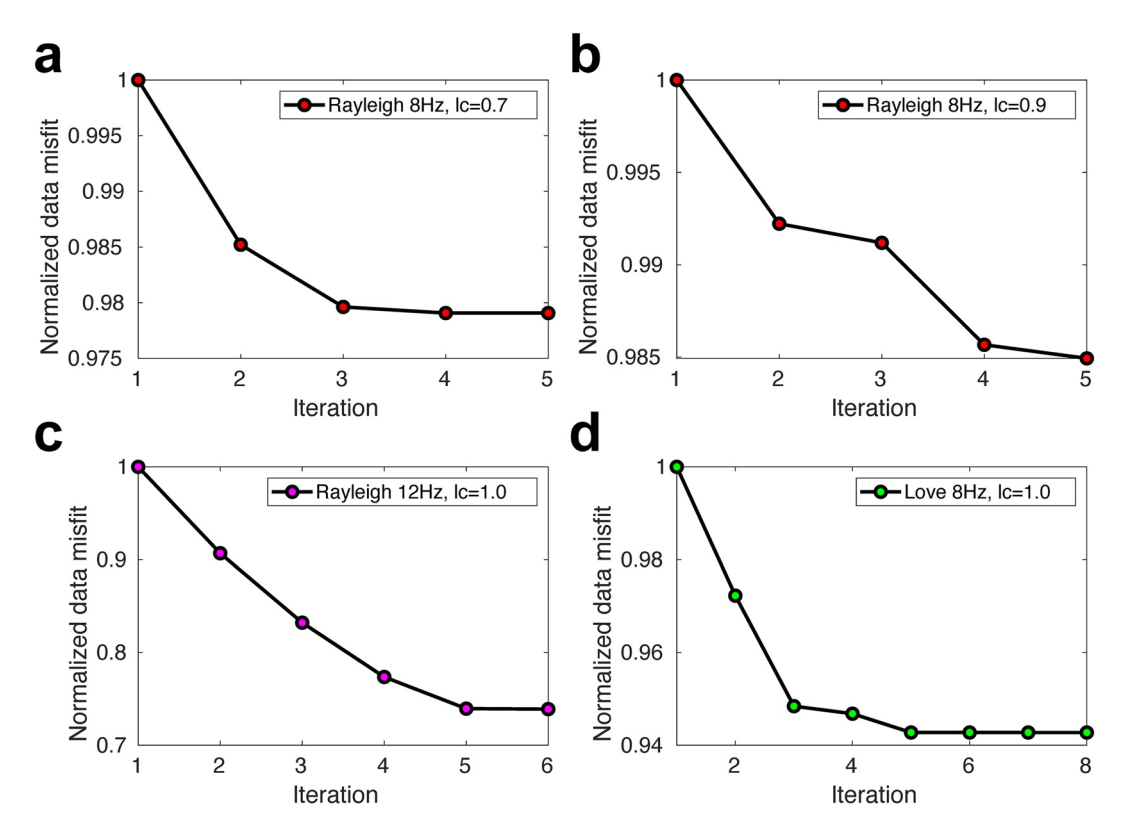


Figure 10. Evolution of the misfit function in four sequential inversion stages. (a) Rayleigh wave inversion centered at 8 Hz with a searching extension of 30% (Z.-D. Zhang & Alkhalifah, 2019a). (b) Rayleigh wave inversion centered at 8 Hz with a searching extension of 10%. (c) Rayleigh wave inversion centered at 12 Hz with a dot-product objective function (Choi & Alkhalifah, 2012). (d) Love wave inversion centered at 8 Hz with a dot-product objective function.

considered in the numerical simulation, such as attenuation and noise. We continue with showing the waveform comparison in Figures 12 and 13. Note that we do not use the waveform difference in our objective function. The accuracy of waveforms calculated from the correlated wavefields is still in debate (Nakata et al., 2013). Instead, we measure the slope of arrivals, which is an indicator of the accuracy of the estimated velocity model. Figures 12a and 13a are the observed ZZ- and ZR-component data, respectively. The initially predicted ZZ and ZR waveforms from the linearly increasing velocity model are shown in Figures 12 and 13b, respectively. We calculate the non-zero lag cross-correlation of the observed and initially predicted ZZ and ZR data shown in Figures 12c and 13c. A black dashed line is added to aid the evaluation of the flatness of correlated traces. The flatness of the cross-correlation functions along traces indicates the accuracy of the inverted velocity model. The side-lobe of the cross-correlation function indicates the accuracy of the dispersion feature of the reconstructed Rayleigh waves from the inverted shear velocity. We ignore the constant time lag since it is related to the origin time of the source wavelet, which will not affect our inversion. The improvement in waveform similarity after inversion is clearly shown in Figures 12d and 13d. A notable difference is that the numerically predicted waveform amplitudes are stronger for high-frequency data, while the observed data seem to have a stronger amplitude for the low-frequency data. Presumably the attenuation that happens in the real Earth can explain such difference, where an opportunity for attenuation factor (Q) estimation exists. The cross-correlation functions shown in Figures 12e and 13e further confirm the improvements in waveform similarity after inversion. The cross-correlation function becomes flat and spiky along traces.

We also show the dispersion spectra of Love waves in Figure 14. The observed Love wave dispersion spectrum is dominated by low-frequency energies as shown in Figure 14a. The inverted dispersion spectrum (Figure 14b) matches the observed one reasonably well at low frequencies (<15 Hz). The finally predicted dispersion spectrum fails to match the observed one at higher frequencies, partially because the dispersion energy is too weak to be utilized. By visually checking the dispersion spectra at high frequencies, we can find that the predicted spectrum has a higher phase velocity than the observed one. Using the general mapping relationship between the

ZHANG ET AL. 11 of 18

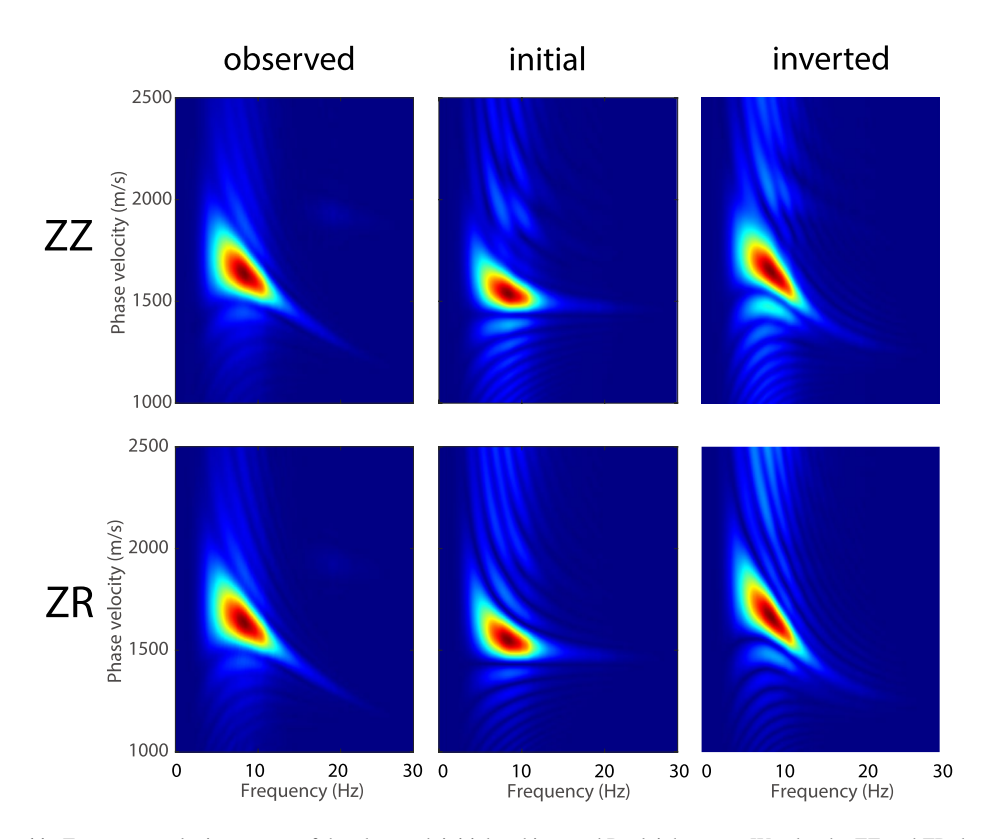


Figure 11. Frequency-velocity spectra of the observed, initial and inverted Rayleigh waves. We plot the ZZ and ZR data for the first virtual source data. The inverted f-v spectra have a better agreement with the observed ones than the initially predicted data.

available frequency and the penetration depth, we anticipate that our estimated Vsh model has a higher velocity than the actual case in the very shallow layer. The waveform data shown in Figure 15a are apparently noisier than ZZ and ZR data. Body waves, including primary arrivals and reflections from a deep layer, are also visually seen. The finally predicted waveform data (Figure 15b) are close to the observed one in terms of the slopes. The cross-correlation function is also flattened along traces (Figure 15c). But we do see some side-lobes of the cross-correlation function, those nearly-flat ones are due to the imperfect prediction for the velocity model and the dipping ones are just crosstalks between the observed body waves and the simulated Love waves. We anticipate that the reflection SH waves marked by the yellow arrow could be from a deep discontinuity, where RTM imaging can help with finding their origins.

8. Reverse Time Migration Imaging Using Reflection SH Waves

Normally, body wave energy is weak and hard to extract from ambient noise, and hence we need extra steps for body-wave extraction (Nakata et al., 2011, 2015). In this data set, because we have transverse components and surface waves are not overlapped to body waves, the reflected SH waves are coherently extracted from the recorded ambient noise by examining several virtual shot gathers. Figures 16a–16c show three example shot gathers with different virtual source locations. We apply a time-selection window to highlight the reflection waves. By stacking the nearby two traces on both sides of the virtual source, we can obtain the so-called zero-offset profile shown in Figure 16d. The two-way traveltime (TWT) of the image is the traveltime of the SH wave from the virtual source to the reflector and then back to the receiver co-located with the virtual source. TWT can be converted to depth by using prior interval velocities. The time-domain image (Figure 16d) shows a dipping reflector that causes the reflections observed in the TT-component data, which is also confirmed by the moveout difference observed in Figure 16b. The (apparent) slope of SH reflection waves on both sides of the virtual source is asymmetric. Since the lateral variation of velocity is mild in the study area, such slope difference is likely caused by the dipping of the reflector. The moveout of traces located at larger *X* (marked by a yellow arrow) indicates a faster apparent velocity caused by the dipping layer's uplifting side. The time-domain zero-offset image provides

ZHANG ET AL. 12 of 18

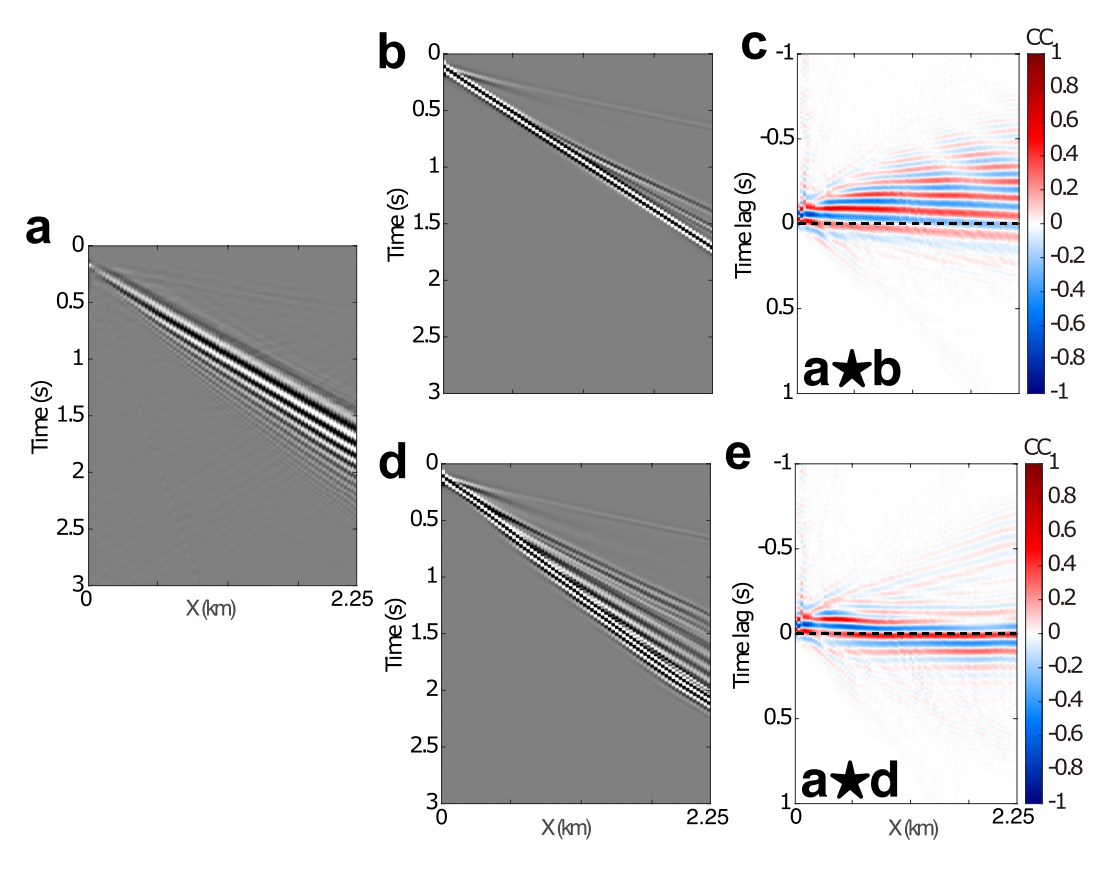


Figure 12. Waveform comparison between the observed and inverted ZZ data. (a) Observed ZZ data after convolution with a Ricker wavelet with a peak frequency of 12 Hz. The frequency content of the f- ν spectrum is determined by the raw virtual sources as shown in Figure 2 and the Ricker wavelet. (b) Initially predicted data and its crosscorrelation with the observed data (c). (d) Finally predicted data and its crosscorrelation with the observed data (e). The black star denotes the correlation operator. A flat and spiky correlation function indicates a good match of predicted and observed seismic waveforms. The dashed black line is a straight reference line.

a first glance of the reflector. The imaging method is robust since it is directly from the observation data. But it cannot provide accurate depth or dipping angle of reflectors.

Here we calculate the RTM image using the time-windowed SH reflections (Nakata et al., 2015). We extend the Vsh model (Figure 7) by flooding with a constant velocity of 1,994 m/s below 150 m and propagating seismic waves using the spectral element method. We scale the velocity value by 0.5 to get the density model, which is an approximation to a derived relationship between velocity and density (Diez et al., 2014). We anticipate that the density error will have a minimal imprint on the velocity estimation due to weak data sensitivity. Figure 17 shows the raw RTM image and its envelope for better visualization. Due to the poor illumination at boundaries and the lack of near-offset reflections (see Figure 16 for evidence), we have a limited range of imaging with high quality. The reflector image is spread in-depth due to the relatively low-frequency range (5–15 Hz) used for imaging. We show the trace-normalized envelope of the raw RTM image in Figure 17b. A solid green line marks a dipping reflector at about 1,700 m depth. The poor data quality interprets a lateral discontinuity marked by the yellow dashed line as imaging artifacts. The lateral depth variation of the imaged reflector is also questionable due to poor data quality. However, the RTM image agrees well with the time-domain image unraveling a dipping reflector.

Reflecting SH wave imaging using ambient-noise data may provide unique illumination to the subsurface. Reflection SH waves are well separated from the surface waves, as shown in this example. PSV or PP reflections largely overlap with surface waves, which prevents their practical use for reflection imaging. Furthermore, SH reflections are purely seismic responses to abrupt changes in shear impedance. By examining the different reactions of *P*- and *S*-wave to the structures in the subsurface, we can predict the physical process of the subsurface. In this study, we did not find clear PP or PSV reflections related to the imaged reflector by searching for possible

ZHANG ET AL. 13 of 18

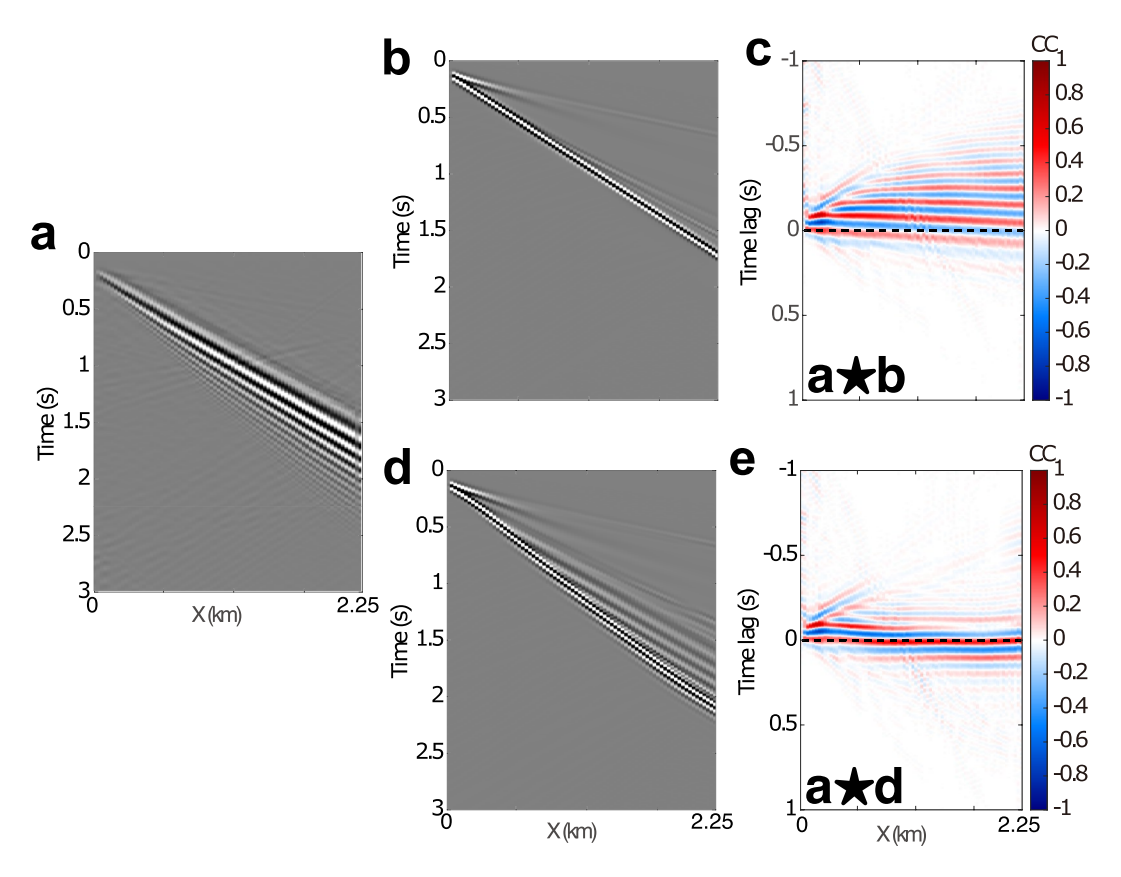


Figure 13. Waveform comparison between the observed and inverted ZR data. (a) Observed ZR data after convolution with a Ricker wavelet with a peak frequency of 12 Hz. (b) Initially predicted data and its crosscorrelation with the observed data (c). (d) Finally predicted data and its crosscorrelation with the observed data (e). The amplitude difference in low- and high-frequency components between the observed and synthetic data may be caused by the attenuation in the real world, which may indicate a method for Q model estimation.

arrival times. We link the reflector to the porosity change of ice at this depth according to the different *P*- and *S*-wave responses (Loh et al., 2017). The inferred porosity change at this depth also agrees with the rapid enlargement of crystals found in the Byrd core (Gow & Williamson, 1976, Figure 3). A more recent ice core study at the WAIS Divide Camp is also available from Fitzpatrick et al. (2014), where they observed a slow increase of mean

grain radius from about 1,750 m and an abrupt reduction after 2,000 m depth during the Antarctic Cold Reversal (e.g., Figure 7).

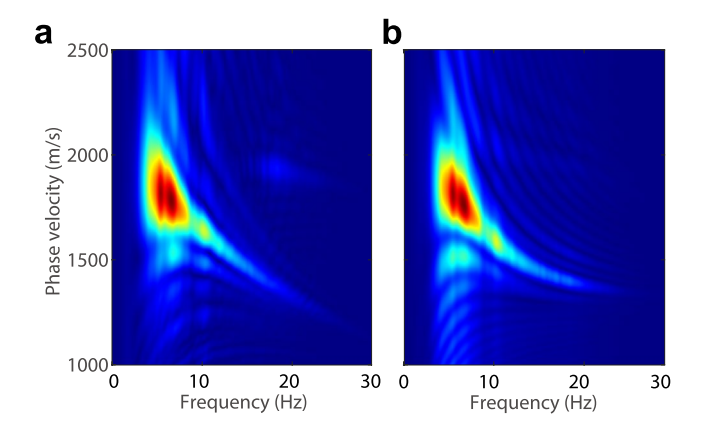


Figure 14. Frequency-velocity spectra of the observed and inverted Love waves. We do not expect an exact match between the observed and synthetic data since we cannot simulate the full physics of wave propagation. A complete data matching indicates a data over-fitting.

9. Discussion: Toward Petrophysical Property Estimation Using P and S Waves

Seismic discontinuities including vertical fractures and horizontal layers of ice-sheets are indicators of its variation in petrophysical property and offer clues to ice dynamics and thermodynamics. The fluid content near the bedrock affects the lubrication of the ice-and-bedrock contact, which is closely related to the stability of ice-sheet (Lai et al., 2020; Lliboutry, 1971). Seismic responses are different for abrupt changes in different petrophysical properties including the fluid content. In oil and gas industry, a combination of *P*- and *S*-wave responses is usually used to infer fluid replacement or matrix change in reservoir characterization. In this study, we investigate the feasibility of using *P*- and *S*-wave responses to infer changes in petrophysical properties of ice. The extracted SH reflections from ambient noise have two main advantages in characterizing the reflectors: (a) they are less overlapped

ZHANG ET AL. 14 of 18

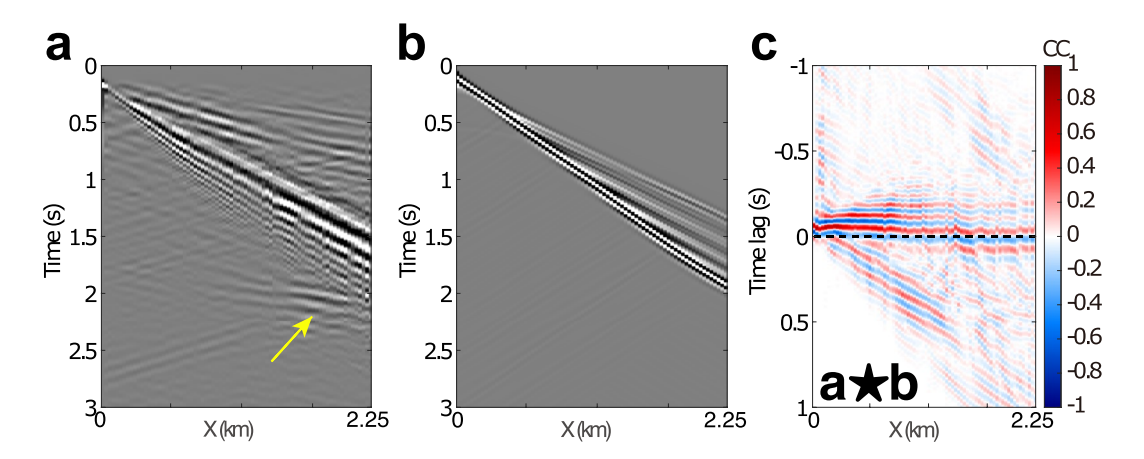


Figure 15. Waveform comparison between the observed and inverted TT data. (a) Observed TT data after convolution with a Ricker wavelet with a peak frequency of 12 Hz. (b) Finally predicted data and its crosscorrelation with the observed data (c). The crosscorrelation is almost flat along traces but is also noisier than those of Rayleigh waves.

with surface waves, and (b) they are decoupled from *P* and SV waves. The SH reflections are helpful in imaging the reflectors. A combination of *P*- and *S*-wave responses can infer the petrophysical change in the subsurface (Loh et al., 2017; Vanorio et al., 2005). Three different combinations of *P*- and *S*-wave responses correspond to three different boundary conditions. To be specific, (a) a variation in rock matrix but not in pore fluid can generate strong *P*- and *S*-wave reflections, (b) No variations in rock matrix but in pore fluid can generate strong *P*-wave but weak *S*-wave reflections, (c) A mineralogy, cementation and porosity condition change can generate weak *P*-wave but strong *S*-wave reflections. In this study, we only observed reflected SH waves from a particular discontinuity, which the porosity change of ice can explain. It is also possible that surface waves hide *P*-wave reflections due to their overlaps in traveltime, but the chance is not high for reflections at near-offsets. Aside from a cross-comparison with *P*-waves, the amplitude variation with offset of SH waves may provide additional

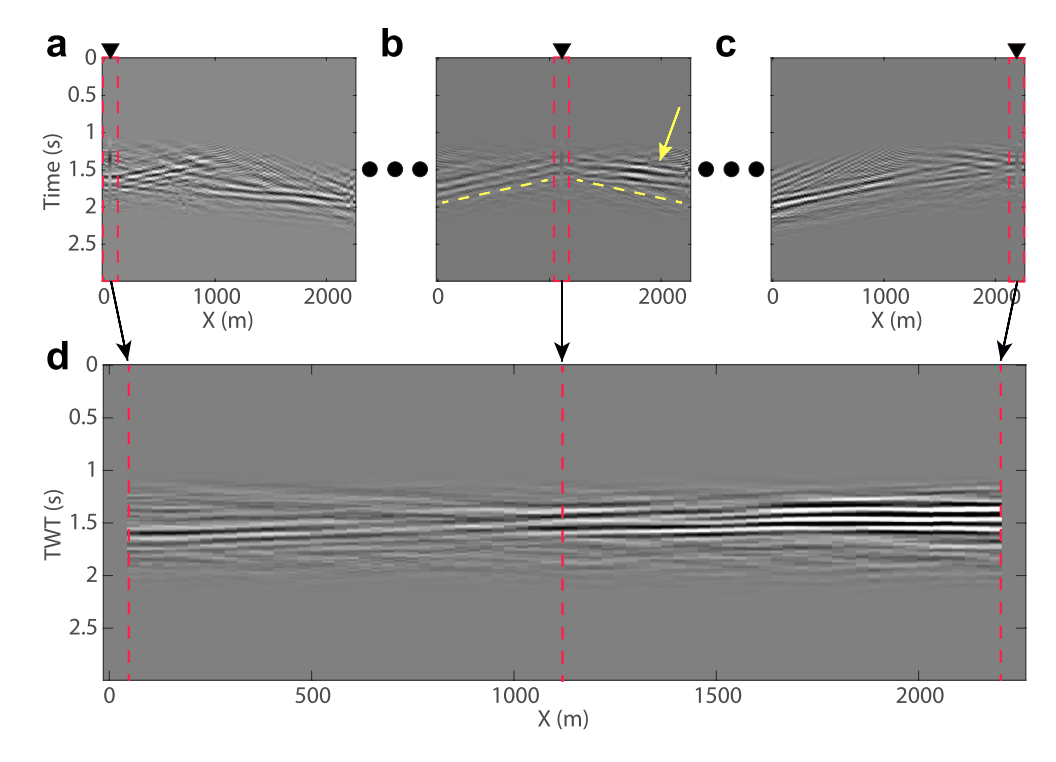


Figure 16. Time-domain zero-offset profiles. Three example virtual shot gathers at different locations (a–c). The zero-offset image extracted from near-offset traces from the virtual shot gathers (d). The red dashed square marks the stacking traces used to generate the zero-offset image.

ZHANG ET AL. 15 of 18

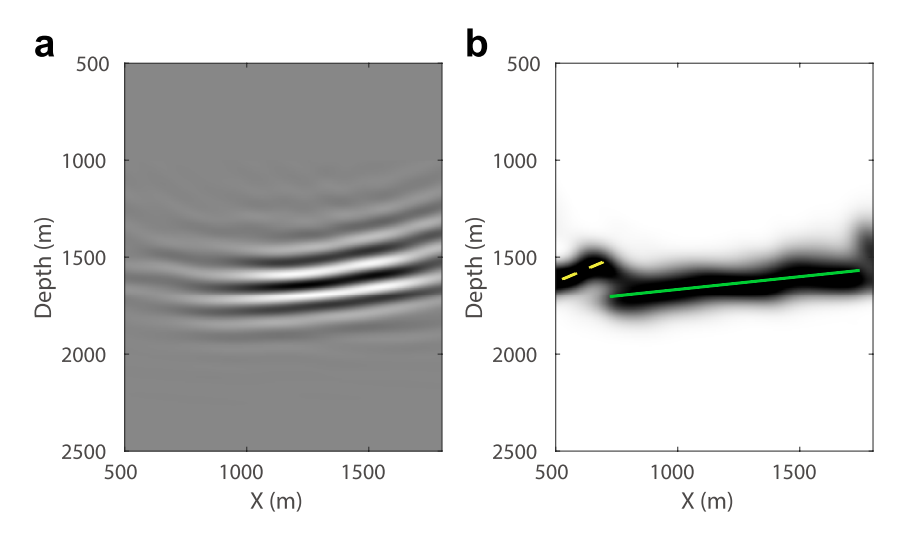


Figure 17. The reverse-time migration image of the reflector (a) and its envelope (d). The image shows the reflector at a depth of around 1,700 m and agrees with the dipping direction as shown in Figure 16. The green line marks the general dipping direction of the imaged reflector.

information about the petrophysical property of the subsurface (Foster et al., 2010). Although we did not observe clear bed reflections from the ambient noise data, we do observe clear englacial and bed reflections from the active-source data (Karplus et al., 2019) similar to those in Horgan et al. (2011), which will be our future work.

10. Conclusions

In this study, we show how seismic imaging can help us estimate the petrophysical parameters of ice and further uncover ice dynamics. The wave equation dispersion spectrum inversion method can provide reliable estimations for heterogeneous shear-wave velocities. Compared with conventional 1D inversion results, our new results also provide additional information about the lateral variation of shear-wave velocities. We further estimate thicknesses of firn-air content and firn from the inverted 2D model. The radial anisotropy of firn and shallow ice derived from the inverted velocities shows a higher resolution than the velocities themselves. A lateral variation is clearly shown and the transition point co-located with the anomaly trace observed from the ZZ data. The inversion uncertainty analysis indicates that the top 200 m of the inverted models are well-resolved. The vanished radial anisotropy below 200 m is likely caused by reduced data sensitivity of Love waves. We also observe SH reflections from the TT data and calculate seismic images of the reflectors using a robust and straightforward time-domain imaging method and a more advanced RTM method. We link the seismic discontinuity to porosity changes at that depth by comparing the *P*- and *S*-wave responses.

Acknowledgments

The authors thank Tariq Alkhalifah for helpful discussions. The authors thank the HPC team at KAUST for providing guidance on using IBEX and Shaheen clusters. The computing for this project was partly performed at the OU Supercomputing Center for Education and Research (OSCER) at the University of Oklahoma (OU). This work is from the Thwaites Interdisciplinary Margin Evolution (TIME) project, a component of the International Thwaites Glacier Collaboration (ITGC). Support from National Science Foundation (NSF: OPP-1739027) and Natural Environment Research Council (NERC: Grant NE/S006788/1), Logistics provided by NSF-U.S. Antarctic Program and NERC-British Antarctic Survey.

Data Availability Statement

The waveform data used in this study can be downloaded from the IRIS Data Management Center (available at https://ds.iris.edu/mda/2E/). The numerical solver for seismic wavefield extrapolation and inversion (SPECFEM2D) is available at https://github.com/geodynamics/specfem2d. The 1 arc-second global relief (SRTM1S) is available at https://doi.org/10.5066/F7PR7TFT.

References

Aster, R. C., & Winberry, J. P. (2017). Glacial seismology. Reports on Progress in Physics, 80(12), 126801. https://doi.org/10.1088/1361-6633/aa8473

Bakulin, A., & Calvert, R. (2005). Virtual shear source: A new method for shear-wave seismic surveys. In SEG Technical Program Expanded Abstracts 2005 (pp. 2633–2636). Society of Exploration Geophysicists.

Battle, M., Severinghaus, J., Sofen, E., Plotkin, D., Orsi, A., Aydin, M., et al. (2011). Controls on the movement and composition of firn air at the West Antarctic ice sheet divide. Atmospheric Chemistry and Physics, 11(21), 11007–11021. https://doi.org/10.5194/acp-11-11007-2011

ZHANG ET AL. 16 of 18



- Bensen, G., Ritzwoller, M., Barmin, M., Levshin, A. L., Lin, F., Moschetti, M., et al. (2007). Processing seismic ambient noise data to obtain reliable broad-band surface wave dispersion measurements. *Geophysical Journal International*, 169(3), 1239–1260. https://doi.org/10.1111/j.1365-246x.2007.03374.x
- Boué, P., Poli, P., Campillo, M., & Roux, P. (2014). Reverberations, coda waves and ambient noise: Correlations at the global scale and retrieval of the deep phases. *Earth and Planetary Science Letters*, 391, 137–145. https://doi.org/10.1016/j.epsl.2014.01.047
- Chaput, J., Aster, R., Karplus, M., & Nakata, N. (2022). Ambient high-frequency seismic surface waves in the firn column of central west Antarctica. *Journal of Glaciology*, 68(270), 1–14. https://doi.org/10.1017/jog.2021.135
- Choi, Y., & Alkhalifah, T. (2012). Application of multi-source waveform inversion to marine streamer data using the global correlation norm. Geophysical Prospecting, 60(4), 748–758. https://doi.org/10.1111/j.1365-2478.2012.01079.x
- Claerbout, J. F. (1971). Toward a unified theory of reflector mapping. Geophysics, 36(3), 467-481. https://doi.org/10.1190/1.1440185
- Conway, H., & Rasmussen, L. (2009). Recent thinning and migration of the Western Divide, central West Antarctica. Geophysical Research Letters, 36(12), L12502. https://doi.org/10.1029/2009gl038072
- Diez, A., Bromirski, P., Gerstoft, P., Stephen, R., Anthony, R., Aster, R., et al. (2016). Ice shelf structure derived from dispersion curve analysis of ambient seismic noise, Ross Ice Shelf, Antarctica. *Geophysical Journal International*, 205(2), 785–795. https://doi.org/10.1093/gji/ggw036
- Diez, A., Eisen, O., Weikusat, I., Eichler, J., Hofstede, C., Bohleber, P., et al. (2014). Influence of ice crystal anisotropy on seismic velocity analysis. *Annals of Glaciology*, 55(67), 97–106. https://doi.org/10.3189/2014aog67a002
- Draganov, D., Campman, X., Thorbecke, J., Verdel, A., & Wapenaar, K. (2009). Reflection images from ambient seismic noise. *Geophysics*, 74(5), A63–A67. https://doi.org/10.1190/1.3193529
- Fitzpatrick, J. J., Voigt, D. E., Fegyveresi, J. M., Stevens, N. T., Spencer, M. K., Cole-Dai, J., et al. (2014). Physical properties of the WAIS Divide ice core. *Journal of Glaciology*, 60(224), 1181–1198. https://doi.org/10.3189/2014jog14j100
- Foster, D. J., Keys, R. G., & Lane, F. D. (2010). Interpretation of AVO anomalies. *Geophysics*, 75(5), 75A3–75A13. https://doi.org/10.1190/1.3467825
- Foti, S., Hollender, F., Garofalo, F., Albarello, D., Asten, M., Bard, P.-Y., et al. (2018). Guidelines for the good practice of surface wave analysis: A product of the InterPACIFIC project. *Bulletin of Earthquake Engineering*, 16(6), 2367–2420. https://doi.org/10.1007/s10518-017-0206-7
- Fu, L., Guo, J., Li, J., Deng, B., Liu, G., Xiao, E., & Chen, X. (2021). Imaging the ice sheet and uppermost crustal structures with a dense linear seismic array in the Larsemann Hills, Prydz Bay, East Antarctica. Seismological Research Letters, 93(1), 288–295. https://doi. org/10.1785/0220210135
- Golden, K., Bennetts, L., Cherkaev, E., Eisenman, I., Feltham, D., Horvat, C., et al. (2020). Modeling sea ice. Notices of the American Mathematical Society, 67(10), 1. https://doi.org/10.1090/noti2171
- Gow, A. J., & Williamson, T. (1976). Rheological implications of the internal structure and crystal fabrics of the West Antarctic ice sheet as revealed by deep core drilling at Byrd Station. *The Geological Society of America Bulletin*, 87(12), 1665–1677. https://doi.org/10.1130/0016-7606(1976)87<1665:riotis>2.0.co:2
- Gu, N., Zhang, H., Nakata, N., & Gao, J. (2021). Fault detection by reflected surface waves based on ambient noise interferometry. *Earthquake Research Advances*, 1(4), 22–27. https://doi.org/10.1016/j.eqrea.2021.100035
- Haney, M. M., & Tsai, V. C. (2017). Perturbational and nonperturbational inversion of Rayleigh-wave velocities. *Geophysics*, 82(3), F15–F28. https://doi.org/10.1190/geo2016-0397.1
- Haskell, N. A. (1953). The dispersion of surface waves on multilayered media. Bulletin of the Seismological Society of America, 43(1), 17–34. https://doi.org/10.1785/bssa0430010017
- Horgan, H. J., Anandakrishnan, S., Alley, R. B., Burkett, P. G., & Peters, L. E. (2011). Englacial seismic reflectivity: Imaging crystal-orientation fabric in West Antarctica. *Journal of Glaciology*, 57(204), 639–650. https://doi.org/10.3189/002214311797409686
- Hu, J., Qiu, H., Zhang, H., & Ben-Zion, Y. (2020). Using deep learning to derive shear-wave velocity models from surface-wave dispersion data. Seismological Research Letters, 91(3), 1738–1751. https://doi.org/10.1785/0220190222
- Jaxybulatov, K., Shapiro, N., Koulakov, I., Mordret, A., Landès, M., & Sens-Schönfelder, C. (2014). A large magmatic sill complex beneath the Toba caldera. Science, 346(6209), 617–619. https://doi.org/10.1126/science.1258582
- Karplus, M. S., Kaip, G., Harder, S. H., Veitch, S. A., Nakata, N., Booth, A. D., et al. (2019). Surface explosives in active-source seismic surveying: Performance and new imaging at the West Antarctic ice sheet divide. In AGU Fall Meeting Abstracts (Vol. 2019, p. NS13A–03).
- Komatitsch, D., & Tromp, J. (1999). Introduction to the spectral element method for three-dimensional seismic wave propagation. *Geophysical Journal International*, 139(3), 806–822. https://doi.org/10.1046/j.1365-246x.1999.00967.x
- Koutnik, M. R., Fudge, T., Conway, H., Waddington, E. D., Neumann, T. A., Cuffey, K. M., et al. (2016). Holocene accumulation and ice flow near the West Antarctic Ice Sheet Divide ice core site. *Journal of Geophysical Research: Earth Surface*, 121(5), 907–924. https://doi. org/10.1002/2015if003668
- Lai, C.-Y., Kingslake, J., Wearing, M. G., Chen, P.-H. C., Gentine, P., Li, H., et al. (2020). Vulnerability of Antarctica's ice shelves to meltwater-driven fracture. Nature, 584(7822), 574–578. https://doi.org/10.1038/s41586-020-2627-8
- Levin, S. A. (1984). Principle of reverse-time migration. Geophysics, 49(5), 581-583. https://doi.org/10.1190/1.1441693
- Li, H., Su, W., Wang, C.-Y., Huang, Z., & Lv, Z. (2010). Ambient noise love wave tomography in the eastern margin of the Tibetan plateau. *Tectonophysics*, 491(1-4), 194-204. https://doi.org/10.1016/j.tecto.2009.12.018
- Li, J., Hanafy, S., Liu, Z., & Schuster, G. T. (2019). Wave-equation dispersion inversion of Love waves. Geophysics, 84(5), R693–R705. https://doi.org/10.1190/geo2018-0039.1
- Lin, F.-C., Tsai, V. C., Schmandt, B., Duputel, Z., & Zhan, Z. (2013). Extracting seismic core phases with array interferometry. Geophysical Research Letters, 40(6), 1049–1053. https://doi.org/10.1002/grl.50237
- Liu, D. C., & Nocedal, J. (1989). On the limited memory BFGS method for large scale optimization. Mathematical Programming, 45(1), 503–528. https://doi.org/10.1007/bf01589116
- Lliboutry, L. (1971). Permeability, brine content and temperature of temperate ice. Journal of Glaciology, 10(58), 15–29. https://doi.org/10.1017/s002214300001296v
- Loh, F. C., Chuah, B. L., Zhou, Z. Y., Cai, J., Gong, X., Yao, J. F., et al. (2017). PS depth imaging to detect clastic reservoirs: Vietnam's first 3D-4-C OBC survey in the Cuu Long Basin. In SEG Technical Program Expanded Abstracts 2017 (pp. 2513–2517). Society of Exploration Geophysicists.
- Luo, Y., Xia, J., Miller, R. D., Xu, Y., Liu, J., & Liu, Q. (2008). Rayleigh-wave dispersive energy imaging using a high-resolution linear Radon transform. *Pure and Applied Geophysics*, 165(5), 903–922. https://doi.org/10.1007/s00024-008-0338-4
- Mecking, R., Köhn, D., Meinecke, M., & Rabbel, W. (2021). Cavity detection by SH-wave full-waveform inversion—A reflection-focused approach. *Geophysics*, 86(3), WA123–WA137. https://doi.org/10.1190/geo2020-0349.1

ZHANG ET AL. 17 of 18



- Meredith, M., Sommerkorn, M., Cassotta, S., Derksen, C., Ekaykin, A., Hollowed, A., et al. (2019). Polar regions. Chapter 3, IPCC special report on the ocean and cryosphere in a changing climate.
- Munneke, P. K., Ligtenberg, S. R., Van Den Broeke, M. R., & Vaughan, D. G. (2014). Firn air depletion as a precursor of Antarctic ice-shelf collapse. *Journal of Glaciology*, 60(220), 205–214. https://doi.org/10.3189/2014jog13j183
- Nakata, N., Chang, J. P., Lawrence, J. F., & Boué, P. (2015). Body wave extraction and tomography at Long Beach, California, with ambient-noise interferometry. *Journal of Geophysical Research: Solid Earth*, 120(2), 1159–1173. https://doi.org/10.1002/2015jb011870
- Nakata, N., Snieder, R., Kuroda, S., Ito, S., Aizawa, T., & Kunimi, T. (2013). Monitoring a building using deconvolution interferometry. I: Earthquake-data analysis. *Bulletin of the Seismological Society of America*, 103(3), 1662–1678. https://doi.org/10.1785/0120120291
- Nakata, N., Snieder, R., Tsuji, T., Larner, K., & Matsuoka, T. (2011). Shear wave imaging from traffic noise using seismic interferometry by cross-coherence. *Geophysics*, 76(6), SA97–SA106. https://doi.org/10.1190/geo2010-0188.1
- Pan, Y., Gao, L., & Bohlen, T. (2021). Random-objective waveform inversion of 3D-9C shallow-seismic field data. *Journal of Geophysical Research: Solid Earth*, 126(9), e2021JB022036. https://doi.org/10.1029/2021jb022036
- Pica, A., Diet, J., & Tarantola, A. (1990). Nonlinear inversion of seismic reflection data in a laterally invariant medium. *Geophysics*, 55(3), 284–292. https://doi.org/10.1190/1.1442836
- Picotti, S., Vuan, A., Carcione, J. M., Horgan, H. J., & Anandakrishnan, S. (2015). Anisotropy and crystalline fabric of Whillans Ice Stream (West Antarctica) inferred from multicomponent seismic data. *Journal of Geophysical Research: Solid Earth*, 120(6), 4237–4262. https://doi.org/10.1002/2014jb011591
- Ringler, A. T., Anthony, R. E., Karplus, M. S., Holland, A. A., & Wilson, D. C. (2018). Laboratory tests of three Z-land Fairfield nodal 5-Hz, three-component sensors. Seismological Research Letters, 89(5), 1601–1608. https://doi.org/10.1785/0220170236
- Roethlisberger, H. (1972). Cold regions science and engineering monograph, section 11-A2a: Seismic exploration in cold regions.
- Sergienko, O. V. (2022). No general stability conditions for marine ice-sheet grounding lines in the presence of feedbacks. *Nature Communications*, 13(1), 1–6. https://doi.org/10.1038/s41467-022-29892-3
- Shapiro, N. M., Campillo, M., Stehly, L., & Ritzwoller, M. H. (2005). High-resolution surface-wave tomography from ambient seismic noise. Science, 307(5715), 1615–1618. https://doi.org/10.1126/science.1108339
- Shearer, P. M. (2019). Introduction to seismology. Cambridge University Press.
- Shen, W., Wiens, D. A., Anandakrishnan, S., Aster, R. C., Gerstoft, P., Bromirski, P. D., et al. (2018). The crust and upper mantle structure of central and West Antarctica from Bayesian inversion of Rayleigh wave and receiver functions. *Journal of Geophysical Research: Solid Earth*, 123(9), 7824–7849. https://doi.org/10.1029/2017jb015346
- Sylvette, B.-C., Cécile, C., Pierre-Yves, B., Fabrice, C., Peter, M., Jozef, K., & Fäh, D. (2006). H/V ratio: A tool for site effects evaluation. Results from 1-D noise simulations. Geophysical Journal International, 167(2), 827–837. https://doi.org/10.1111/j.1365-246x.2006.03154.x
- Vanorio, T., Virieux, J., Capuano, P., & Russo, G. (2005). Three-dimensional seismic tomography from P wave and S wave microearthquake travel times and rock physics characterization of the Campi Flegrei Caldera. *Journal of Geophysical Research*, 110(B3), B03201. https://doi. org/10.1029/2004jb003102
- Vigh, D., Jiao, K., Watts, D., & Sun, D. (2014). Elastic full-waveform inversion application using multicomponent measurements of seismic data collection. Geophysics, 79(2), R63–R77. https://doi.org/10.1190/geo2013-0055.1
- Woolery, E. W., Street, R. L., Wang, Z., & Harris, J. B. (1993). Near-surface deformation in the New Madrid Seismic zone as imaged by high resolution SH-wave seismic methods. *Geophysical Research Letters*, 20(15), 1615–1618. https://doi.org/10.1029/93gl01658
- Yang, Y., Ritzwoller, M. H., Levshin, A. L., & Shapiro, N. M. (2007). Ambient noise Rayleigh wave tomography across Europe. *Geophysical Journal International*, 168(1), 259–274. https://doi.org/10.1111/j.1365-246x.2006.03203.x
- Young, T. J., Martín, C., Christoffersen, P., Schroeder, D. M., Tulaczyk, S. M., & Dawson, E. J. (2021). Rapid and accurate polarimetric radar measurements of ice crystal fabric orientation at the Western Antarctic Ice Sheet (WAIS) Divide ice core site. *The Cryosphere*, 15(8), 4117–4133. https://doi.org/10.5194/tc-15-4117-2021
- Zhang, S. X., Wang, Y., Zhou, H.-W., & Chan, L. S. (2009). Dispersion splitting of Rayleigh waves in layered azimuthally anisotropic media. *Journal of Applied Geophysics*, 67(2), 130–142. https://doi.org/10.1016/j.jappgeo.2008.10.008
- Zhang, Z.-D., Alajami, M., & Alkhalifah, T. (2020). Wave-equation dispersion spectrum inversion for near-surface characterization using fibre-optics acquisition. Geophysical Journal International, 222(2), 907–918. https://doi.org/10.1093/gji/ggaa211
- Zhang, Z.-D., & Alkhalifah, T. (2019a). Local-crosscorrelation elastic full-waveform inversion. Geophysics, 84(6), R897–R908. https://doi.org/10.1190/geo2018-0660.1
- Zhang, Z.-D., & Alkhalifah, T. (2019b). Wave-equation Rayleigh-wave dispersion inversion using fundamental and higher modes. *Geophysics*, 84(4), EN57–EN65. https://doi.org/10.1190/geo2018-0506.1
- Zhang, Z.-D., Liu, Y., & Schuster, G. (2015). Wave equation inversion of skeletonized surface waves. In SEG Technical Program Expanded Abstracts 2015 (pp. 2391–2395). Society of Exploration Geophysicists.
- Zhang, Z.-D., Saygin, E., He, L., & Alkhalifah, T. (2021). Rayleigh wave dispersion spectrum inversion across scales. *Surveys in Geophysics*, 42(6), 1281–1303. https://doi.org/10.1007/s10712-021-09667-z
- Zigone, D., Ben-Zion, Y., Campillo, M., & Roux, P. (2015). Seismic tomography of the Southern California plate boundary region from noise-based Rayleigh and Love waves. Pure and Applied Geophysics, 172(5), 1007–1032. https://doi.org/10.1007/s00024-014-0872-1

ZHANG ET AL. 18 of 18